Gooch *et al. Journal of Electric Propulsion* (2026) 5:8
https://doi.org/10.1007/s44205-026-00184-y

Journal of Electric Propulsion

RESEARCH

Open Access

A simplified numerical procedure for the characterization of an ionic liquid meniscus with evaporation

Ford Gooch[1*], John Cater[2], Kean Aw[1] and Rajnish Sharma[1]

*Correspondence:
Ford Gooch
fgoo638@aucklanduni.ac.nz
[1]Department of Mechanical Engineering, University of Auckland, Princes Street, Auckland 1010, New Zealand
[2]Department of Engineering, Computer and Mathematical Sciences, Auckland University of Technology, Wellesley Street East, Auckland 1010, New Zealand

Abstract

Ionic liquid pure-ion electrospray propulsion may be a pivotal technology for micro-satellite propulsion. Extensive modeling is required to understand the underlying physical interactions. However, combining the coupled electric fields, transport mechanisms, and heating effects in a generalized numerical model remains challenging. An investigation conducted by Coffman allowed for insight into the dominant physical processes. This model was further refined, and a second implementation substantially improved computational performance and numerical stability. Unfortunately, these studies still struggled with the significant computational cost. Drawing from the results in Coffman's previous work and integrating the later stability enhancements, the present work achieves a more robust and computationally efficient implementation. Here, the increased numerical stability of the revised model permits a larger range of parameter values to be used, and allows for data collection at practical capillary sizes, opening the door to experimental validation. Using the revised model, the thermodynamic properties of the ionic liquid are varied to explore the effect of diffusivity on the meniscus, which indicates increased numerical stability for liquids with higher diffusivity.

Keywords Electrohydrodynamics, Electrospray propulsion, Ionic liquids, Pure-ion emission, Numerical modeling

Introduction

Electrospray thrusters operate by accelerating ions or droplets across a potential difference [1]. These thrusters offer advantages primarily to microsatellites, due to their relatively low power consumption (below 5 W), high specific impulse and bipolarity. The main limitation is low thrust; however, this can be mitigated by array operation [2]. Unlike traditional plasma-based thrusters, the molecules and/or ions are extracted directly from liquid menisci via strong electric fields [3]. During operation, a liquid meniscus sits at the top of a capillary, porous tip, or externally wetted needle. These menisci are stressed via strong electric fields. This stress leads to Taylor cone formation, which balances electrical and interfacial forces. This cone releases a jet that breaks into a 'spray', primarily composed of droplets. The composition of this spray is influenced by the liquid's conductivity, the flow rate, geometric parameters, and the extraction field.

As an emitter's flow rate decreases, and given an appropriate working liquid, the emitter will eventually extract individual ions in combination with droplets [4]. Under specific conditions (low flow rates and high electric field strength), ion evaporation can occur without droplets [5]. Only a few liquids, including liquid metals, concentrated aqueous acids, and ionic liquids support this distinct electrohydrodynamic charge emission. Understanding the interaction of charged droplet emission (known as the 'cone-jet mode') in electric fields is well-documented [6–8], but modeling the field emission of pure-ion sources remains challenging [9].

The first attempt at modeling pure-ion ionic liquid electrospray sources employed a leaky dielectric method to examine a constant volume droplet subjected to an external electric field, where they explicitly modeled the electric fields, surface charge depletion, activated emission, Stokes flow, and the surface tension of the meniscus [10]. This research critiqued the traditional Taylor cone shape, and suggested instability in the pure-ion regime.

The work was expanded by Coffman [11], who removed the constant volume restrictions, introduced temperature fluctuations, and included an actively fed capillary source with hydraulic impedance. This study identified two distinct operating regimes for pure-ion electrospray; a group of non-emitting 'egg' solutions that reproduce the equipotential and hydrostatic profiles found in foundational studies of stressed dielectric droplets [12], and a second solution group of emitting cone-like solutions replicating the trends of ionic liquid ion electrospray emitters, providing a form of validation.

In 2019, another study further built on Coffman's model [13, 14], and the more relevant second solution group. This study discovered additional zones of operation and identified stability boundaries. Gallud's modeling was a substantial extension regarding efficiency, numerical stability and computational cost. The Coffman model and Gallud's extension of it remain the most comprehensive models for pure-ion electrospray sources to date. However, these models are computationally expensive, increasingly so at large meniscus sizes (above $\approx 2.5\mu\mathrm{m}$ for all liquids). Furthermore, these models are often numerically unstable for conditions that correspond to menisci that have been experimentally observed, indicating that physical solutions are out of numerical reach.

In the present work, a simplified version of the leaky dielectric model is presented. The problem is generalized as a free-volume liquid column attached to a flat plate that is electrically biased relative to a upstream surface. The liquid column has a fixed contact point with the plate and thus a prescribed radius, while, at the same time, the meniscus curvature is free to change. The revision is a steady-state numerical model, solving the Taylor-Melcher leaky dielectric problem.

In an extension of the previously explored parameter space, diffusivity is investigated. Varying diffusivity permits the modeling of larger menisci, potentially permitting future validation, and allows investigation of ionic liquid properties.

Problem definition

For a capillary emitter, the liquid meniscus is described as initially flat [11]. During operation, this meniscus is charged relative to the extractor plate. The applied potential difference establishes electric fields between the meniscus and the extractor plate, concentrating charge at the surface of the meniscus and creating a force on the now-charged meniscus. Once this force is strong enough to disturb the initial equilibrium, the meniscus ‘snaps over’ into the traditional Taylor cone, which is pinned at the internal radius of the capillary. This Taylor cone balances the surface tension, electric traction, and liquid stress, amplifying the electric fields at its tip, and extracting ions directly from the charged meniscus. Importantly, the precise shape of the meniscus is unknown; this shape affects the electric field’s strength and directionality, and thus the force balance.

As charged ions leave the meniscus, the surface charge is depleted, i.e. the meniscus is no longer electrically relaxed [11]. The degree of charge depletion is the result of the equilibrium between emission and the two charge transport mechanisms: convection of charged particles along the meniscus surface, and Ohmic conduction. The Ohmic conduction of charge also causes Ohmic heating, altering the properties of the liquid. As ions accelerate, their charge alters the electric fields, an effect known as space charge.

As liquid is extracted from the meniscus, there is a resulting liquid inflow at a defined pressure from a reservoir feed. This pressurized liquid moves though a feeding system, which has hydraulic resistance, affecting the pressure experienced at the meniscus. Therefore any change in flow results in a change in the hydrostatic pressure at the meniscus [11]. The overall goal of the revised model is to find the meniscus shape that provides an equilibrium balance between the pressure and determine the emission properties.

The revised model uses an axisymmetric domain. There are three sub-domains and one key interface in the model space, as shown in Fig. 1. The liquid sub-domain is represented by the superscript l for various force components; this domain is defined by the plate’s location and the meniscus’s shape. The vacuum domain is represented by the superscript, v. The plate, represented by the subscript p, is a rectangle of thickness z_p, and length $r_p - b_0$ (the domain radius minus the capillary radius), originating at the bottom of the overarching domain. The upstream electrode is perpendicular to the feeding plate, at a height of z_0, with an infinitely small thickness at the edge of the overarching domain. The downstream electrode is biased relative to the upstream electrode to establish the electric fields.

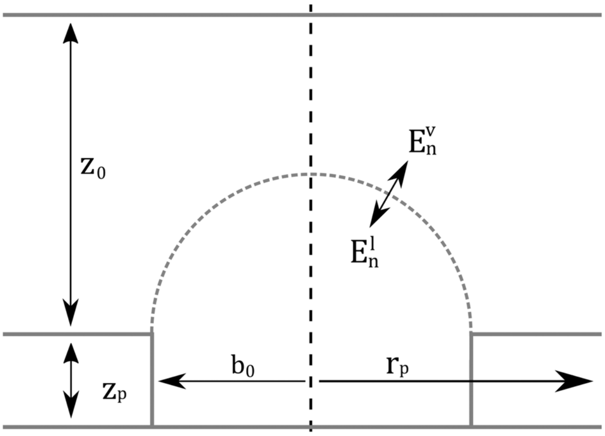

Fig. 1 The domain of the generalized ionic liquid ion electrospray meniscus problem, showing the liquid, plate and electric subdomains. E^v and E^l represent the electric fields within the vacuum and liquid subdomains respectively

Simplifications

The revised model in this work neglects the effect of space charge, which has been found to contribute less than 1% of the pressure balance, making its inclusion in the overall balance unnecessary [11]. This neglect aligns with Coffman's 2016 and Gallud's 2019 models [11, 14]. In 2023, Gallud introduced a form of space charge; however, this inclusion generally confirmed the original assumption that space charge is unlikely to significantly affect the overall meniscus [15].

For momentum exchange, Newton's third law requires that for every particle expelled, an opposing force is exerted on the meniscus, resulting in a "recoil". However, momentum analysis shows that this effect contributes roughly 10^{-6} % to the total pressure balance at the meniscus. Therefore, it is also neglected, consistent with all three major models [11, 14, 15].

In this work, the convection term from the current conservation equation is removed [11]. This term represents the quantity of charge replenished by charged particles moving along the meniscus surface towards the tip of the meniscus via liquid motion. This process may be necessary for cone-jet electrospray. However, Coffman's 2016 results demonstrated that charge convection is two orders of magnitude smaller than Ohmic conduction, and thus unnecessary to include in the overall analysis.

Viscous forces are also neglected in the revised model. In the Coffman model, peak dynamic viscous forces accounted for less than 0.2 units of non-dimensional pressure at a non-dimensional radius ($\hat{r}$) of 0.05 [11]. This value trended towards zero near the fixed contact point. This can be compared to a peak of 10 non-dimensional units of pressure for electric traction forces. Note that the hydrostatic pressure from the feed system contributes to more of the force balance and is constant over the entire meniscus. Dynamic liquid forces were, on average, two orders of magnitude smaller than the hydrostatic pressure. These results suggest that neglecting viscous forces will have only minor effects on the overall force balance. The non-dimensionalization scheme is explained in Sect. 3.7.

For energy conservation, specifically within the heat transfer solver described in Sect. 3.3, both viscous dissipation and mixing are neglected in the governing equation, resulting in energy input arising solely from Ohmic heating. Because the Reynolds number is approximately 10^{-2}, convective and viscous contributions to energy transport can be assumed to be negligible in this flow regime [11]. This again aligns with Coffman's 2016 and Gallud's 2019 models [14].

As all effects pertaining to the liquid motion have been neglected, it is unnecessary in this work to determine the liquid motion within the meniscus itself, and therefore momentum conservation does not need to be considered. As seen in the results, this makes the solution procedure more linear and less computationally expensive. This results in a revised model that broadly encompasses the same physics as the previous models from Gallud and Coffman, with the exception of a dynamic flow and the convection of charged particles [11, 14]. Assuming the meniscus to be hydrostatic results in a less accurate numerical model, as known effects are neglected. However, the results show that these omissions have a limited impact on solutions and that the added numerical stability expands the range of attainable solutions.

Theoretical background

Electric field

For the electric field formulation, the conventional method is to consider the liquid as quasi-neutral and the surrounding vacuum and plate as neutral [9]; this allows for the use of the Laplace equations in vacuum while also allowing charge depletion at the meniscus [11]. This method may not accurately represent the charge separation layer, however, this simplification captures the relevant physical behavior [15]. Therefore, the Laplace equations govern both the vacuum and plate domains,

$$\nabla^2 \Phi^v = 0, \tag{1}$$

$$\nabla^2 \Phi^p = 0, \tag{2}$$

where Φ is the electric potential.

The liquid region couples active emission and Ohmic conduction. To ensure consistency throughout the domain, the conduction within the liquid is governed by the steady-state charge conservation law,

$$\nabla \cdot j = 0. \tag{3}$$

where j is the current density vector.

Furthermore, within the liquid bulk, current density is governed by Ohmic conduction,

$$j = kE^l, \tag{4}$$

where E^l is the electric field in the liquid domain. When the conductivity k is constant, this leads to a linear relationship between current density and electric field, enabling the current to be inferred directly from the electric field without explicitly solving transport equations.

As identified in the problem definition, this Ohmic conduction causes Ohmic heating, changing liquid properties. This is primarily in the form of temperature-dependent conductivity, modelled via a linear approximation [15]:

$$k = k_0 + k' \left(T - T_0\right), \tag{5}$$

where T_0 is the reference temperature, T is the temperature of the liquid at a specific point, k_0 is the electrical conductivity at the reference temperature, and k' is the linear change in conductivity with each degree of temperature increase.

When this temperature-dependent conductivity is introduced, spatial gradients in conductivity can result in a non-zero divergence of the current density, implying an accumulation of charge. To accommodate temperature-dependent conductivity while using standard electrostatic solvers to approximate current, Coffman and Gallud introduce an effective pseudo-space-charge density into Gauss's law [11, 14]. This formulation numerically captures the influence of spatially varying conductivity on the electric field to preserve charge conservation in the system.

The required pseudo-charge due to the temperature dependence of conductivity can be defined via [11],

$$\rho_f = -\epsilon_0 \epsilon_r \frac{k' \left(\nabla T\right) \cdot E^l}{k_0 + k' \Delta T}, \tag{6}$$

where ϵ_0 is the dielectric constant, and ϵ_r is the relative permittivity.

Therefore, although the model remains quasi-neutral within the liquid bulk, Gauss's law and the electrostatic potential equation are used rather than the Laplace equation:

$$\nabla \cdot D = \rho_v, \tag{7}$$

$$E = -\nabla\Phi. \tag{8}$$

Noting that,

$$D = \epsilon_0 \epsilon_r E, \tag{9}$$

therefore,

$$\nabla \cdot (\varepsilon_0 \varepsilon_r \nabla\Phi) = \rho_v, \tag{10}$$

where D is the electric displacement field, ρ_v is the volume charge density, and E is the electric field. Furthermore, the domains are sized to isolate the meniscus,

$$\hat{r_p} \gg 1, \tag{11}$$

$$\hat{z_0} \gg 1, \tag{12}$$

where r_p and z_0 are defined as shown in Fig. 1, and non-dimensionalized by the capillary radius b_0.

The material properties of the plate are relevant to isolate the meniscus from dielectric effects. The revised model uses an ideal dielectric to prevent fields of substance from being generated.

To initialize the imposed electric field, a voltage is applied to the upstream electrode with a value corresponding to the specified non-dimensional electric field (E_0),

$$\Phi^v \left(z = z_0\right) = -V = E_0 E_c z_0, \tag{13}$$

where z_0 is shown in Fig. 1. All remaining boundaries within the electric system (excluding the meniscus and the axisymmetric condition at $r = 0$) are set to the reference potential ($0V$).

Liquid-vacuum electric interface (meniscus)

The liquid-vacuum interface, or the meniscus, is where equilibrium is established in the revised model. As the surface charge at the meniscus may be depleted, it is described by the jump condition,

$$\sigma = \epsilon_0 E_n^v - \epsilon_0 \epsilon_r E_n^l, \tag{14}$$

where σ is the surface charge, and the electric fields are denoted by their superscripts.

Active emission can be modeled by the kinetic evaporation law [16],

$$j_e = \sigma \frac{k_B T}{h} exp\left[\frac{-1}{k_B T}\left(\Delta G - \sqrt{\frac{q^3 E_n^v}{4\pi\epsilon_0}}\right)\right], \tag{15}$$

where j_e is the emitted current, k_B is the Boltzmann constant, h is the Planck constant, T is the temperature, ΔG is the solvation energy, and q is the charge of the emitted ion, which is assumed to be an elemental charge.

The meniscus surface is defined by a balance in the normal direction [15]:

$$n \cdot (\tau_e - \tau_m) \cdot n - \gamma \nabla \cdot n = 0, \tag{16}$$

where $-\gamma \nabla \cdot n$ is the surface tension, τ_e is the electric traction determined via Maxwell's equations, τ_m is the hydrostatic stress of the meniscus (in a 2D tensor), which is defined further on in this work, n is the normal vector of the meniscus contour.

Heat transfer

The effect of liquid heating on emission is significant, potentially responsible for more than 20% of emission [11]. For the revised model, changes in conductivity are modeled by the linear approximation introduced in Eq. 5.

Heat transfer within the liquid bulk is governed by the stationary heat equation:

$$\nabla \cdot q = Q, \tag{17}$$

where q is the heat flux vector, and Q represents general thermal sources, respectively. Energy input from Ohmic heating, required to solve this heat transfer system, is defined as [14]:

$$Q = \left[k_0 + k' \left(T - T_0\right)\right] E^l \cdot E^l, \tag{18}$$

The meniscus boundary is defined as adiabatic, relying upon the approximation of thermal insulation:

$$\hat{n} \cdot \nabla T = 0, \tag{19}$$

where $\hat{n}$ is the unit normal vector, all remaining boundaries, except the axisymmetric one, are held at the reference temperature.

Analytical pressure difference

For a hydrostatic meniscus, two liquid pressures must be considered: the reference (or reservoir) liquid pressure (P_r), and the pressure loss due to hydraulic resistance. The consideration of reference pressure is straightforward; it is simply considered as the initial hydrostatic pressure.

The pressure loss due to liquid flow (P_d) is more challenging, as the flow rate must be determined before analytical consideration of the hydraulic resistance of the (unmodeled) feed system. The current density j is integrated over the rotated surface area of the meniscus to determine the total current I emitted by the meniscus. Assuming an average charge-to-mass ratio and a propellant density value, the flow rate Q of the meniscus is given by,

$$Q = \frac{I}{\rho \left(q/m\right)}. \tag{20}$$

where the term q/m is the charge-to-mass ratio, and ρ is the liquid's density. The pressure drop due to hydraulic resistance is modeled by Poiseuille flow, as the Reynolds number is estimated to be approximately 10^{-2} [11]. This allows for an analytical solution,

$$P_d = -\frac{IR_h}{\rho\,(q/m)}, \tag{21}$$

where P_d is the drop in pressure and R_h is the hydraulic resistance of the imagined feed setup (such as a capillary tube). The hydraulic impedance is defined by the non-dimensional scheme introduced in Sect. 3.7.

Thus, the total hydrostatic pressure at the meniscus due to the feed system can be expressed as:

$$P_f = P_r - P_d = P_r - \frac{IR_h}{\rho\,(q/m)}, \tag{22}$$

where P_f is the overall feed pressure. This overall feed pressure acts equally in both the r and z directions of the previously introduced two-dimensional τ_m tensor.

Emission magnitudes

For non-dimensionalization, the determination of the order of magnitudes of the emission is necessary. Assumptions during these derivations are solely used to determine the non-dimensionalization scheme. Using Eq. 15, the conditions for maximum or 'copious' emission can be determined [11]. This allows for the determination of the critical electric field:

$$E^* = \frac{4\pi\epsilon_0(\triangle G)^2}{q^3}, \tag{23}$$

where q is the charge of each extracted ion.

During copious emission, we can assume that the central area of the meniscus that is emitting is limited to a spherical cap of critical curvature r^*, characterized by a radius from the central axis [11]. Assuming vanishingly small tangential forces within this critical curvature, the appropriate surface tension expression is balanced relative to the Maxwell tensor in the normal direction, and can be written as,

$$\frac{1}{2}\epsilon_0\left[\left(E_n^v\right)^2 - \epsilon_r\left(E_n^l\right)^2\right] \sim \frac{2\gamma}{r^*}, \tag{24}$$

where γ is the surface tension coefficient, and E_n^v, and E_n^l represent the normal electric fields on the vacuum and liquid sides of the meniscus contour, respectively. If the entire area within this critical curvature is at the critical field strength, the meniscus can be modeled by the conventional jump condition for an idealized surface charge. Assuming that conduction within the meniscus is the dominant transport mechanism, and using Eq. 15, the current balance is given by,

$$j_e = \epsilon_0\left(E_n^v - \epsilon_r E_n^l\right)\frac{k_BT}{h} \times \exp\left[\frac{-1}{k_BT}\left(\Delta G - \sqrt{\frac{q^3E_n^v}{4\pi\epsilon_0}}\right)\right]. \tag{25}$$

Further simplification via the substitution of Ohmic conduction ($j_e = kE^l$), and rearranging for E_n^l, gives the following,

$$E_n^l = \frac{E_n^v/\epsilon_r}{1 + \frac{kh}{\epsilon_0\epsilon_r k_B T} exp\left[\frac{-1}{k_B T}\left(\Delta G - \sqrt{\frac{q^3 E_n^v}{4\pi\epsilon_0}}\right)\right]}. \tag{26}$$

The dimensionless group $kh/(\epsilon_0\epsilon_r k_B T)$ can be evaluated using common ionic liquid properties near room temperature ($k \sim 1S/m, \epsilon_r \sim 10^1 - 10^2$) for a value of approximately 10^{-3} [11]. Since the section of meniscus within the critical curvature is experiencing copious emission, this leads to the exponent value trending towards zero. Permitting the following approximation [11],

$$E_n^l = E_n^v/\epsilon_r. \tag{27}$$

Equation 26 can therefore then be simplified to:

$$\frac{1}{2}\epsilon_0 \left(E^*\right)^2 \left(\frac{\epsilon_r - 1}{\epsilon_r}\right) \sim \frac{2\gamma}{r^*}. \tag{28}$$

Rearranging provides a value for the critical radius of emission (r^*):

$$r^* \sim \frac{4\gamma}{\epsilon_0 \left(E^*\right)^2} = \frac{q^6\gamma}{4\pi^2\epsilon_0^3 \left(\Delta G\right)^4}. \tag{29}$$

Equations 28 and 29 assume that the region of evaporation is modeled as a spherical cap. Thus, the calculation of the characteristic current I^* becomes:

$$I^* = j^*A = kE_n^*A = \frac{kE^*}{\epsilon_r}2\pi(r^*)^2 = \frac{32\pi k\gamma^2}{\epsilon_0^2\epsilon_r E^{*2}}, \tag{30}$$

where the current density j^* is governed by Ohm's law, and A is the surface area of the emitting cap. For common ionic liquids, this produces a value in the order of 50-500nA [11].

Force balance metrics

The following expansions are useful when comparing to the results of previous models. The normal electric stress on the meniscus is determined by the Maxwell tensor [11]:

$$\tau_n^e = \frac{1}{2}\epsilon_0 \left[\left(E_n^v\right)^2 - \epsilon_r \left(E_n^l\right)^2\right] + \frac{1}{2}\epsilon_0 \left(\epsilon_r - 1\right) E_t^2, \tag{31}$$

where τ_n^e represents the electric traction in the normal direction, and E_t is the electric field in the tangential direction.

The surface tension can be expressed in terms of the converged meniscus profile [11, 14]:

$$\tau_n^{st} = -\gamma \left[\frac{\left(1 + \dot{y}^2\right)\dot{y} + r \cdot \ddot{y}}{r\left(1 + \dot{y}^2\right)^{3/2}}\right], \tag{32}$$

where τ_n^{st} is the normal surface tension pressure, *n* is the normal vector, *y* is the is the meniscus profiles height as a function of radial position and, $\dot{y}$, $\ddot{y}$ are the first and second derivatives of *y* with respect to *r*, respectively.

Non-dimensionalization

Lengths are scaled by the radius of the capillary (b_0), pressure by the capillary pressure (P_c), electric fields by a simplified critical emission field (E_c), current densities and current by the related emission (based on Eq. 30), and temperature by reference T_0. The non-dimensionalized parameters are [11, 14],

$$\hat{L} = \frac{L}{b_0}, \quad \hat{A} = \frac{A}{b_0^2}, \quad \hat{P} = \frac{P}{P_c}, \quad \hat{E} = \frac{E}{E_c}, \quad \hat{j} = \frac{j}{k_0 E_c}, \quad \hat{I} = \frac{I}{k_0 E_c b_0^2}, \quad \hat{\sigma} = \frac{\sigma}{\epsilon_0 E_c}, \quad \hat{T} = \frac{T}{T_0}.$$

The critical electric field is the field at the onset of copious emission and is simplified as:

$$E_c = \sqrt{\frac{4\gamma}{\epsilon_0 b_0}}. \tag{33}$$

The capillary pressure is defined by:

$$P_c = \frac{2\gamma}{b_0}. \tag{34}$$

Considering a system using a known liquid isolated at electrically infinity leaves a four-dimensional parameter space as investigated previously [11, 14]. For a specific solution, the parameters are a combination of a non-dimensional electric field (E_0), a non-dimensional reference pressure ($\hat{P}_r$), a *B* value (a measure of capillary radius) and a characteristic hydraulic impedance C_R (based on the dimensioned hydraulic impedance R_h). The *B* ratio (often appearing as B^{-1}) is a ratio of the characteristic emitting radius of the Taylor cone divided by the contact radius.

$$B = \frac{r^*}{b_0}, \tag{35}$$

$$C_R = \frac{k_0 E_c b_0^3 R_h}{2\gamma\rho\,(q/m)}, \tag{36}$$

where R_h is the hydraulic impedance.

Further non-dimensional numbers could be defined based on liquid properties, however it is simpler to state representative dimensioned values [11, 17]; $\epsilon_r = 10$, $k_0 = 1$ S/m, $k' = 0.04$ S/m-K, $q/m = 10^6$ C/kg, $\rho = 10^3$kg/m^3, $c_p = 1500$ J/kg-K, $k_T = 0.2$ W/m-K, $\gamma = 0.05$ N/m, $\Delta G = 1$ eV, and $T_0 = 300$ K. These reference values are used for the remainder of this work, unless otherwise stated.

Summary of governing equations

For reference the governing equations and boundary conditions are presented for each sub-domain (Vacuum, Liquid, and Plate) and the key interface (Liquid-Vacuum). They are as follows:

Vacuum domain

$$\nabla^2 \Phi^v = 0, \tag{37}$$

$$\Phi^v \left(z = z_0\right) = -V = E_0 E_c z_0, \tag{38}$$

$$\left.\frac{\partial \Phi}{\partial r}\right|_{r=0} = 0, \tag{39}$$

where Eq. 37 governs throughout the vacuum domain, and Eqs. 38 and 39 denote the boundary conditions on the upper and axisymmetric boundary, respectively.

Liquid domain

$$\nabla \cdot j = 0. \tag{40}$$

$$\nabla \cdot \left(\varepsilon_0 \varepsilon_r \nabla \Phi\right) = \rho_v, \tag{41}$$

$$\rho_f = -\epsilon_0 \epsilon_r \frac{k' \left(\nabla T\right) \cdot E^l}{k_0 + k' \Delta T}. \tag{42}$$

$$\left.\frac{\partial \Phi}{\partial r}\right|_{r=0} = 0, \tag{43}$$

$$\nabla \cdot q = Q + Q_p + Q_{vd}, \tag{44}$$

$$\left.\frac{\partial T}{\partial r}\right|_{r=0} = 0, \tag{45}$$

$$\dot{q} = \left[k_0 + k' \left(T - T_0\right)\right] E^l \cdot E^l, \tag{46}$$

$$k = k_0 + k' \Delta T, \tag{47}$$

where Eqs. 40, 41, 42, 44, 46 and 47 govern throughout the domain. Equations 43 and 45 denote the axisymmetric boundary conditions.

Liquid-vacuum interface

$$\sigma = \epsilon_0 E_n^v - \epsilon_0 \epsilon_r E_n^l, \tag{48}$$

$$j_e = \sigma \frac{k_B T}{h} exp \left[\frac{-1}{k_B T} \left(\Delta G - \sqrt{\frac{q^3 E_n^v}{4 \pi \epsilon_0}}\right)\right] \tag{49}$$

$$j_e = k E_n^l, \tag{50}$$

$$I = \int_{\hat{r}=0}^{\hat{r}=b_0} j_e \, dA, \tag{51}$$

$$n \cdot \left(\tau_e - \tau_m\right) \cdot n - \gamma \nabla \cdot n = 0, \tag{52}$$

$$\tau_m = P_f = P_r - P_d = P_r - \frac{IR_h}{\rho\,(q/m)}, \tag{53}$$

$$\hat{n} \cdot \nabla T = 0, \tag{54}$$

where all equations are enforced at the interface.

Plate domain

$$\nabla^2 \Phi^p = 0, \tag{55}$$

$$\dot{\Phi}^p \big|_{r=0} = 0 \tag{56}$$

where $\dot{\Phi}^p$ is the derivative of the electric potential with respect to *r*. Equation 55 governs the entire domain, and Eq. 56 denotes the axisymmetric condition.

Numerical procedure

To manage the coupled physics of the system, the governing equations are divided among three physics interfaces: an electric finite element analysis (FEA), a heat transfer FEA, and a generalized partial differential equation (PDE) interface. The electric FEA is governed by Eqs. 37-43, 48–50, 55, and 56. The heat transfer FEA is governed by Eqs. 44-47, and 54. The PDE solver determines a meniscus profile by minimizing the residual of Eq. 53, with implementation details provided in Sect. 4.4. Equations 51, and 53 are considered analytically. An outline of the solution process is shown in Fig. 2.

General procedure

The input parameters include the non-dimensional electric field, reference pressure, hydraulic impedance and emitter geometry. The general numerical procedure then continues as follows: (1) the revised model populates an initial guess of the meniscus shape, (2) the model calls the electric field FEA solver, which solves for the emission from the surface of the meniscus, the surface charge, and the electric fields in the vacuum and liquid bulk, (3) the model exports the data from the electric FEA solver and calls the heat transfer FEA solver, solving for a temperature, and thus conductivity, distribution within the liquid bulk, (4) the model exports the data from the heat transfer FEA solver, and determines all analytical pressures required for propagation, (5) the model calls the PDE solver, which determines a meniscus profile that minimizes the residual pressure using the values from the previous solvers, (6) the new meniscus profile is exported from the PDE solver, and a residual to the initial meniscus profile is calculated, (7) the model evaluates this meniscus residual, either propagating the meniscus or classifying the meniscus as converged, (8) processes 2–7 are repeated until the meniscus profile is considered converged.

The revised model is implemented with COMSOL version 5.4 with MATLAB live link R2020b, allowing transition between the numerical, analytical and finite element methods [18, 19]. Notably, while the discussion of the modeling is presented in non-dimensional units, COMSOL requires dimensioned inputs.

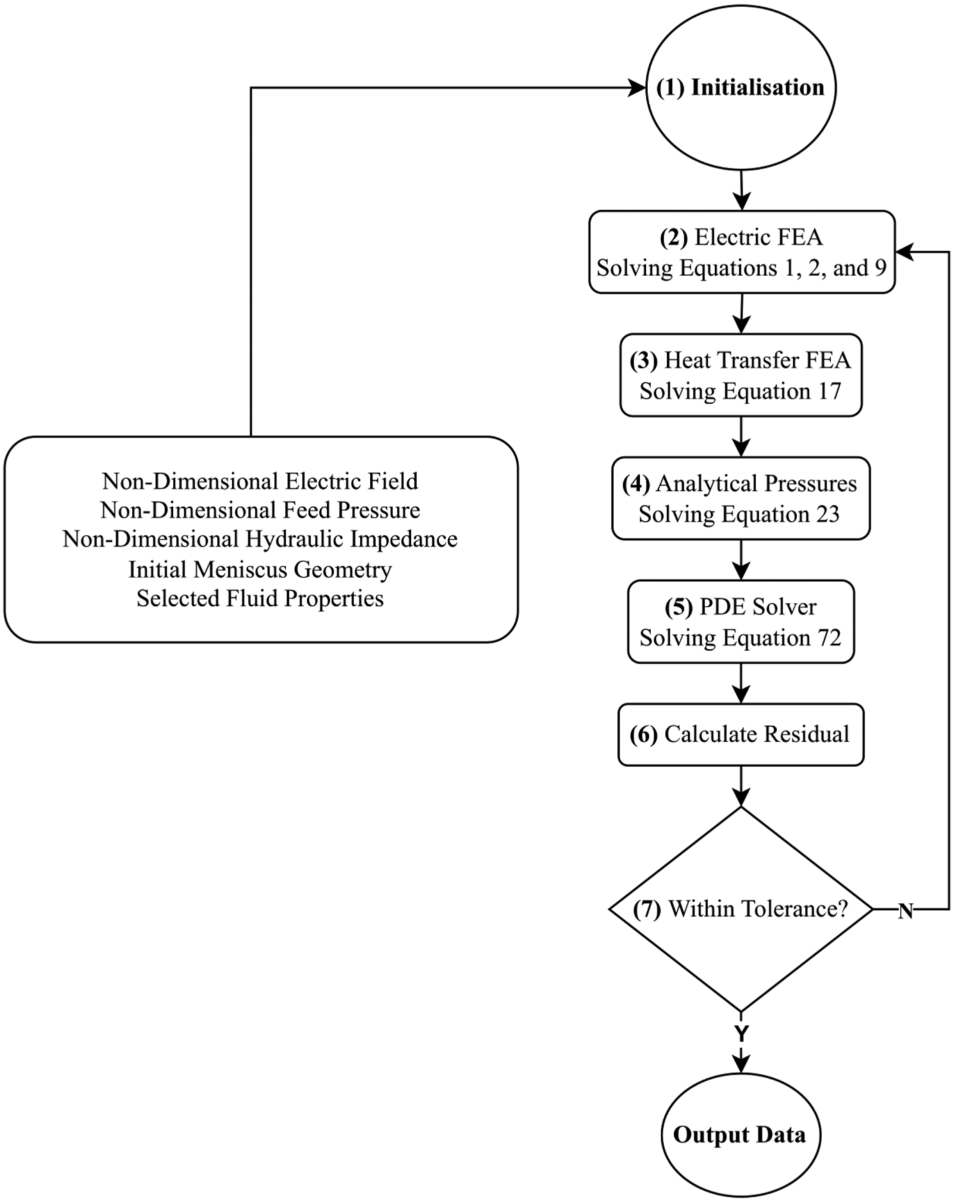

Fig. 2 The revised model solution process

Electric field FEA solver

The electric field FEA uses the axisymmetric model space shown in Fig. 1. The governing equations and boundary conditions are likewise imposed during the electric solver initialization. Special treatment of the meniscus's surface charge and emission is required for a solution, this process is outlined below.

The meniscus has a surface charge that varies along its radial length. This surface charge is specified via the jump condition (Eq. 14). When the FEA model executes, the solver determines the vacuum electric fields via the Laplace equations and the interactions of the dielectrics. From Eq. 15, it then determines the current emitted via kinetic evaporation, determining the current density over the meniscus contour. This emission requires an inflow of charge; this is determined via the liquid's conductivity and Eq.

4, which therefore specifies the liquid's internal electric fields and once again, surface charge.

The main complexity of this FEA is in how the equations are coupled. For example, if it is assumed that full relaxation of the surface charge occurs (i.e. surface charge is a maximum), then kinetic emission would also be at a maximum, and therefore, the internal electric fields would be as strong as possible. These internal electric fields result in the depletion of the surface charge via the jump condition, therefore reducing emission. Consequently, an equilibrium solution involves not just the vacuum electric fields, but also the ion emission (which itself is electrically dependent).

The simplest solution method is to assume that the coupling is limited and calculate emission by assuming a fully relaxed meniscus. However, previous work indicates this would be an over-simplified solution, as Coffman and Gallud both experienced depletion values above 50%, with a consequential emission decrease by the same proportion (Eq. 15) [11, 14].

The approach selected to address this was to separate the calculation of emission into a linked PDE solver within the single electric FEA COMSOL model. By using a segregated solver, COMSOL was directed to solve the initial model, whose surface charge is defined only by the vacuum's normal electric field, and then for all future calculations the surface charge is defined via vacuum's normal electric field subtracted from the calculated emission from the previous iteration:

$$\sigma = \epsilon_0 E_n^v - \epsilon_0 \epsilon_r \frac{1}{k} j_e^{i-1}. \tag{57}$$

This equation is based on the jump condition (Eq. 14). COMSOL continues this process until the fields have converged. This method removes any circular dependency within COMSOL's factorization and allows the solver to produce converged surface charge and electric field values with limited external input.

Heat transfer FEA solver

The heat transfer FEA domain also uses a axisymmetric grid, however only contains the liquid bulk. The governing equations and boundary conditions are again imposed during initialization, with the energy input from Ohmic heating the same as in Sect. 3.3. Ohmic heating is determined using the electric fields calculated by the electric FEA solver. After the heat transfer solver is complete, COMSOL outputs a map of the temperature throughout the liquid subdomain.

This temperature map is an input into the next iteration of the electric FEA, such that the changes in electrical conductivity and temperature are included in the emission analysis. Therefore the temperature input to the electric FEA is from the previous iteration of the heat transfer FEA. Due to the slight difference between iterations, this allows for the reduction of error within the heat transfer solution, eventually reaching convergence without specific intervention [11].

Once the heat transfer solver computes the temperature distribution and passes it to the subsequent electric solvers, these solvers must incorporate an effective space charge density into the electrostatic formulation to maintain charge conservation [11]. This is similar to space charge ($\nabla \cdot E = \rho_f/\epsilon$), and thus can be implemented as a charge density map:

Table 1 Mesh generation parameters for the heat transfer solver

Constraint Name	Definition	Value
h_{max}	Maximum allowable element size (m)	$b_0/25$
h_{min}	Minimum allowable element size (m)	10^{-11}
h_{grad}	Maximum allowable growth rate	1.25
h_{curve}	Maximum allowable element size along a curved boundary	0.005

Table 2 Mesh generation parameters for the electric field solver

Constraint Name	Definition	Value
h_{max}	Maximum allowable element size (m)	$b_0/4$
h_{min}	Minimum allowable element size (m)	10^{-11}
h_{grad}	Maximum allowable growth rate	1.25
h_{curve}	Maximum allowable element size along a curved boundary	0.01

$$\rho_f\left(r,z\right) = -\epsilon_0\epsilon_r \frac{k'\left(\nabla T\right)\cdot E^l}{k_0 + k'\Delta T}. \tag{58}$$

The revised model uses two different meshes for the electric and heat transfer FEAs. The simpler mesh is the heat transfer mesh. COMSOL's in-built meshing engine discretizes the heat transfer domain into a triangular mesh. This model uses the same parameters as Coffman, as shown in Tables 1 and 2. Using the same mesh parameters and settings ensures that their selection does not unduly influence the results or subsequent comparisons. Furthermore, additional refinement produces negligible changes.

The electric FEA mesh uses a single adaption step in addition to the triangular discretization from COMSOL. By providing COMSOL with a reference value of E^2, COMSOL distributes additional elements to the mesh to reduce the solution's residual error [11].

PDE solver and meniscus propagation

After convergence of the electric solution, the heat transfer solution, and the calculation of all analytical pressures, the revised model determines whether the meniscus is in equilibrium and, if not, propagate the meniscus contour.

To iteratively change the meniscus shape, the revised model utilizes Galllud's PDE formulation [14]. This PDE was formulated via a pseudo-continuous residual force balance in the normal direction, and aims to minimize the total normal pressure residual by modifying the meniscus contour, and thus surface tension:

For a given $\hat{\tau}_m^i$ and $\hat{\tau}_e^i$, find $\hat{n}^{i+1}$ such that $J_+(n^{i+1})$ is a minimum for:

$$J_+(n^{i+1}) = \frac{1}{2}\int_0^1 (R_+^{i+1})^2 d\hat{r}, \tag{59}$$

where,

$$R_+^{i+1} = \hat{n}^{i+1}\cdot(\hat{\tau}_e^i - \hat{\tau}_m^i)\cdot\hat{n}^{i+1} - \frac{1}{2}\nabla\cdot\hat{n}^{i+1}, \tag{60}$$

where R_+^{i+1} is a continuous residual force balance in the normal direction and $\hat{n}^{i+1}$ represents the unit normal vector of the meniscus contour. The superscript i represents the current iteration and, $i+1$ is the next iteration. The expansion of the residual forces is evident in the right-hand side of Eq. 60. These residual forces are the vector forms of the surface tension ($-\frac{1}{2}\nabla\cdot\hat{n}^{i+1}$), electric traction ($\hat{\tau}_e^i$), and a combined value representing the liquid forces ($\hat{\tau}_m^i$), respectively.

For an equilibrium, it is expected that the residual values should approach zero:

$$\hat{\tau}_e^{i+1} \approx \hat{\tau}_e^i; \quad \hat{\tau}_m^{i+1} \approx \hat{\tau}_m^i; \quad R_+^{i+1} \approx R_+^i \approx 0.$$

Following this initial definition of the minimization problem, Gallud used an arbitrary transformation (Eq. 61) and replaced the normal components in the residual balance with their analytical expressions (Eqs. 62 and 63). Symbols $\dot{\hat{y}}$, and $\ddot{\hat{y}}$ are the first derivative of height with respect to radius, and the second derivative with respect to radius, respectively.

$$R_{++}^{i+1} = 2\left[1+\left(\dot{\hat{y}}^{i+1}\right)^2\right]^{\frac{3}{2}} R_+^{i+1}, \tag{61}$$

$$n = \frac{1}{\sqrt{1+\left(\dot{\hat{y}}^{i+1}\right)^2}}\left(-\dot{\hat{y}}^{i+1}, 1\right), \tag{62}$$

$$\nabla\cdot n = \frac{\left[1+\left(\dot{\hat{y}}^{i+1}\right)^2\right]\dot{\hat{y}}^{i+1} + r\ddot{\hat{y}}^{i+1}}{r\left[1+\left(\dot{\hat{y}}^{i+1}\right)^2\right]^{\frac{3}{2}}}. \tag{63}$$

The scalar forces *a*, *b*, and *c* are defined in a two-dimensional tensor to simplify notation. The values are determined from the previous FEA solutions:

$$\hat{\tau}_e^i - \hat{\tau}_m^i = \begin{pmatrix} a & b \\ b & c \end{pmatrix}, \tag{64}$$

$$a = (\hat{E}_r^v)^2 - (\hat{E}_z^v)^2 - \epsilon_r\left((\hat{E}_r^l)^2 - (\hat{E}_z^l)^2\right) + \hat{P}_f, \tag{65}$$

$$b = 2\hat{E}_r^v\hat{E}_z^v - \epsilon_r(2\hat{E}_r^l\hat{E}_z^l), \tag{66}$$

$$c = (\hat{E}_z^v)^2 - (\hat{E}_r^v)^2 - \epsilon_r\left((\hat{E}_z^l)^2 - (\hat{E}_r^l)^2\right) + \hat{P}_f. \tag{67}$$

The two-dimensional tensor can be interpreted as the pressure balance at the meniscus, excluding the surface tension. The electric components are simply from Maxwell's equations, and the liquid forces are analytical calculations.

This leads to the following expanded equation:

$$R_{++}^{i+1}(\dot{\hat{y}}^{i+1}, \ddot{\hat{y}}^{i+1}) = 2[1+(\dot{\hat{y}}^{i+1})^2]^{\frac{1}{2}}[a(\dot{\hat{y}}^{i+1})^2 - 2b\dot{\hat{y}}^{i+1} + c] + \frac{[1+(\dot{\hat{y}}^{i+1})^2]\dot{\hat{y}}^{i+1}}{\hat{r}} + \ddot{\hat{y}}^{i+1}, \tag{68}$$

and the corresponding functional minimization problem used by Gallud,

$$J_{++}(\hat{r}, \dot{\hat{y}}^{i+1}, \ddot{\hat{y}}^{i+1}) = \frac{1}{2}\int_0^1 (R_{++}^{i+1})^2 d\hat{r}. \tag{69}$$

Through the functional minimization Gallud determined the meniscus profile that minimized the pressure residual. The new meniscus profile was compared to the initial profile to calculate a meniscus residual, then updated:

$$\hat{y}^{i+1} = \hat{y}^{i} + \beta \Delta \hat{y}, \tag{70}$$

The propagation or numerical relaxation coefficient β is used the same way as Coffman's value [20].

In this work, it is not necessary for Eq. 68 to be solved by using the functional minimization problem posed by Gallud in Eq. 69, as the revised model already makes use of COMSOL. Implementing Eq. 68 in a separate FEA PDE solver, which automatically computes the weak form to minimize the residual value, is relatively simple. This FEA solver uses a one-dimensional solution domain of unit length, which is governed by Eq. 68. The domain has a gradient of zero at the meniscus tip due to the axisymmetric condition, and an R_{++}^{i+1} value of zero at the contact point as the meniscus is pinned.

The Newtonian solver in COMSOL finds the solution to Eq. 68, solving for the gradient ($\dot{\hat{y}}$). This value is then integrated within MATLAB for the meniscus profile, permitting the calculation of a meniscus residual and the propagation of the meniscus profile via Eq. 70.

The convergence criterion at every point on the meniscus is given by:

$$\frac{\Delta y(\hat{r})}{b_0} < tol. \tag{71}$$

A value of *tol* = 0.001 is used. This condition is a departure from both Coffman and Gallud, who used a tolerance of 0.01 for non-dimensional pressure changes in the normal direction (including dynamic liquid force, electric traction, and surface tension) rather than the meniscus profile [11, 14]. The tighter tolerance is used to increase the resolution of results during parameter sweeps. The revised model is considered to have failed when no solution within tolerance is found within 1000 iterations. Considering the tolerance in terms of maximum meniscus deviation removes the possible influence of Coffman and Gallud's 'contact line singularity' on the ability of the numerical scheme to converge.

When the revised model fails to solve for a particular set of parameters, it was found to be for one of two reasons; either the oscillating error cannot be decreased below the required tolerance level, or a phenomenon known as current runaway [14]. Current runaway occurs at small values of B and early in the iteration process. This happens when the first electric iteration provides a relatively high emission solution, that creates a significant heating effect, thus increasing the emission further from high Ohmic heating. This continues via a feedback loop until a COMSOL solver cannot find a solution, normally in the electric field solver. This is the dominant failure condition for the revised model.

Increases in mesh density and decreases in the meniscus relaxation parameter β can mitigate both failure mechanisms. However, the solution tends to fail as soon as the non-dimensional electric field increases (or B decreases). Consequently, a fixed value of β simplifies parameter sweeps and allows quick analysis. The relaxation coefficient was chosen to be 0.1 to increase computational speed; this is larger than the relaxation coefficient used by Coffman (0.05) [11]. This may introduce numerical instability to the system, but verification tests demonstrate that comparable accuracy has been retained. As in previous models, the selection of β has a negligible effect on the final results [11, 15].

At low values of dimensionless electric field (0.5–0.7, depending on other parameters), a non-emitting meniscus equilibrium can be reached, though for the same parameters an emitting equilibrium also exists [11]. Furthermore, the COMSOL solvers fail immediately if the initial position is too far from equilibrium, consequently a well-defined initial position is important. The revised model makes use of the initial condition outlined by Coffman [11].

This initial shape is defined by the following two equations:

$$\hat{\tau}_{st} = \begin{cases} 50, & \text{while } \frac{\cos\theta}{2r} \geq 50 \\ \frac{\cos\theta}{2r}, & \text{otherwise.} \end{cases}$$

Here, the surface tension is limited to a non-dimensional pressure of 50. This ensures that the tip is not too 'sharp' near the axis of symmetry. Outside this region, Coffman chose a cone angle of 60 degrees. An initial temperature map, set at the reference temperature, is also used.

However, at larger meniscus radii (smaller values of B), the permissible initial position of the meniscus becomes more constrained. At these values, the previous position, adapted from Coffman, is unsuitable. In this case, it is better to use the closest previous solution for both the initial meniscus shape and initial temperature.

Model verification and validation

This work has access to two well-defined results for verification [11, 14]. However, the results are still limited to trend matching for physical validation, as there are limited available experimental data sets. Therefore, the following comparisons are made [11]:

- Comparisons to single solution emission metrics from previous models. This will demonstrate that the equilibrium solver and emission metrics are operating as expected, while showing that the simplifications have had a limited effect on the revised models' solutions [11, 14].
- Consistency with the physical principles experienced in previous models: a non-evaporative lower branch, an intermediate or pulsating regime, steady evaporation for large menisci, $I - V$ linearity, $I - B^{-1}$ proportionality, $I - C_R^{-1}$ proportionality, and a relationship between stability and the contact line. The trend validations will demonstrate that the revised model is at least as physically relevant as the previous models. [11, 14].

Parameter variation

The revised model has four parameters, of these the most commonly varied in physical experiments are E_0 and B [21]. Both hydraulic impedance and reference pressure can be varied, but in more recent physical experiments, a zero reference pressure is imposed. This choice is consistent with emitter designs in which no pressure drives the liquid flow, as well as with other numerical simulations in the field [11, 14, 22]. The hydraulic impedance remains constant at 10^3 to 10^4, consistent with the minimum proposed [23].

As a result, the parameter sweeps by Coffman and Gallud investigate a two-dimensional parameter space of E_0 and B, with no reference pressure, repeated for hydraulic impedances of 10^3 and 10^4 to provide a broad understanding of possible solutions. These solution spaces are repeated with the revised model for comparison.

Performance characterization

Comparing the revised model to the previous implementation from Gallud is a convenient way to characterize its performance [14]. Gallud displays the performance of a more computationally efficient version of the Coffman model, including the initial conditions, average computational time per iteration, and the number of iterations required for a solution. These solutions are repeated with the revised model in this work.

For these comparisons, the revised tolerance was increased to the same value as Gallud and Coffman (0.01). The tolerance of the revised model is stated in terms of the largest residual error of the meniscus height; in contrast, Gallud utilizes the maximum pressure method. Although these are not directly analogous, they measure essentially the same movement/residual of the meniscus contour, as set out by Eq. 68. For all terminated solutions presented from the revised model, the termination conditions used by Coffman and Gallud were also checked and found to be within the previous models' stated tolerance.

Thermodynamic properties

In an extension of the previously explored parameter space, diffusivity and thermal properties are varied to determine their effect on emitted current. Variations in these thermal properties are likely to affect emission behavior by altering the temperature, which in turn modifies the electrical conductivity. Coffman and Gallud made use of reference properties for heat capacity at constant pressure ($c_p = 1500$ J/kg-K) and for thermal conductivity ($k_T = 0.2\ \mathrm{W/m\text{-}K}$) [11, 14]. However, both these reference properties differ from those of the most commonly used propellant by a factor of 3 ($c_p \sim 4000$ J/kg-K, $k_T \sim 0.6\ \mathrm{W/m\text{-}K}$) [24].

Investigation of the two-dimensional parameter space use the combined non-dimensional parameter, thermal diffusivity, defined in Eq. 72,

$$\alpha = \frac{k_T}{\rho c_p}. \tag{72}$$

Using the results from this investigation, this work presents a solution at the more commonly used $10\mu\mathrm{m}$ capillary size. This demonstrates that the revised model can predict the performance of realizable physical experiments.

Results

Comparisons to earlier work

The single solution results from the revised model are shown in Figs. 3, 4, and 5, in the form of a prescribed attachment point (B), with standard ionic liquid properties, a characteristic hydraulic impedance, and reference pressure. Figure 3 also presents a comparison to Gallud's implementation. The difference between the revised model and Coffman's model's single solution results is small [11].

The non-dimensional surface charge and meniscus profile have RMS differences of 0.0048 and 0.0125, respectively. As with the comparison to Gallud, the non-dimensional surface charge exhibits the largest discrepancy at the tip of the meniscus, likely due to the less extreme curvature of the revised models' meniscus, a consequence of the neglect of dynamic liquid stress [14]. Feed pressure values are constant along the meniscus' curve and thus can be compared directly; for the single solution parameters, the difference is 1.0%. Without access to the raw data, the best temperature comparison becomes tip temperature, where

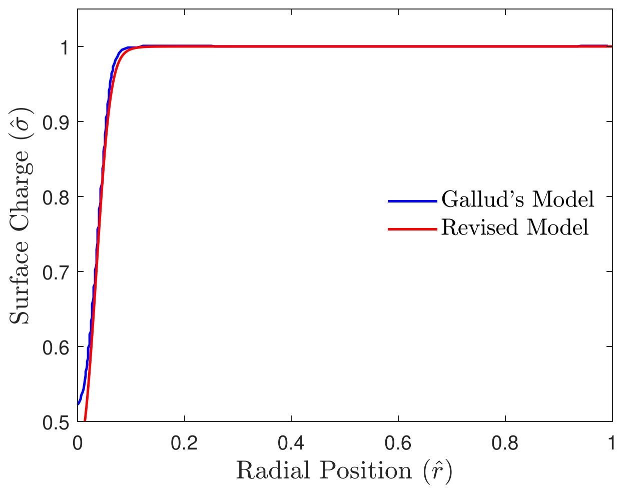

Fig. 3 The non-dimensional surface charge for both Gallud's model and the revised model at $E_0 = 1.0$, B=0.047, $C_R = 10^3$, and $\hat{P}_r = 0$. Surface charge ($\hat{\sigma}$) is non-dimensionalized by the expected surface charge for a fully relaxed meniscus ($\epsilon_0 E_n$). The symbol $\hat{r}$ is the non-dimensional radial position along the meniscus. The figure shows close agreement between the two implementations. Data are extracted from Figs. 4–2 [14]

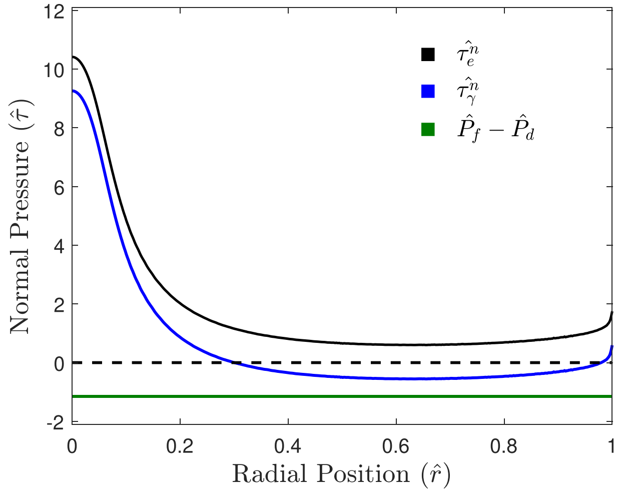

Fig. 4 The non-dimensional pressure ($\hat{\tau}$) at the meniscus from the revised model at $E_0 = 1.0$, B=0.047, $C_R = 10^3$, and $\hat{P}_r = 0$. $\hat{P}_f - \hat{P}_d$ is constant over the meniscus

the temperature is expected to be at a maximum. The difference in absolute tip temperature is 1.7%. Overall, the agreement between the revised and both previous models is relatively close, with the meniscus profile varying no more than 0.02 non-dimensional units. As the previous models considered the solution converged once per-solution deviation was less than 1%, this shows good agreement. This agreement allows the verification of the underlying physics of the revised model.

Physical behavior

A key part of the validation of both previous models was the use of an order of magnitude validation, which shows current emission with increasing field strength (for various *B* ratios) [11, 14]. Consequently, Figs. 6 and 7 present the order of magnitude for the revised model at hydraulic impedances of 10^3 and 10^4. Figure 8 presents the order of

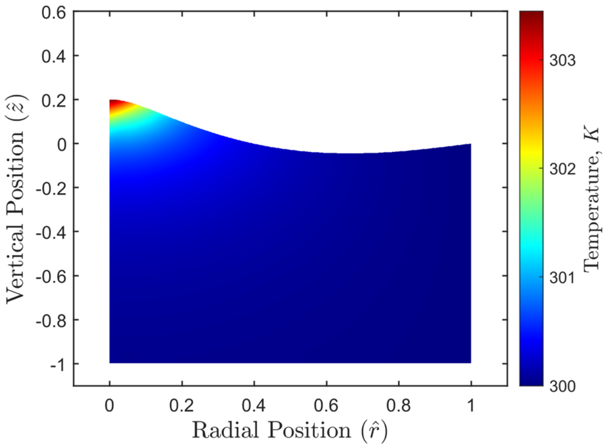

Fig. 5 The temperature distribution in the liquid domain from the revised model at $E_0 = 1.0$, B=0.047, $C_R = 10^3$, and $\hat{P}_r = 0$. The shape of the meniscus is shown as the boundary of the coloured region. The increasing color gradient near the tip indicates higher Ohmic heating, and thus higher temperature. The symbol $\hat{z}$ is the non-dimensional vertical position

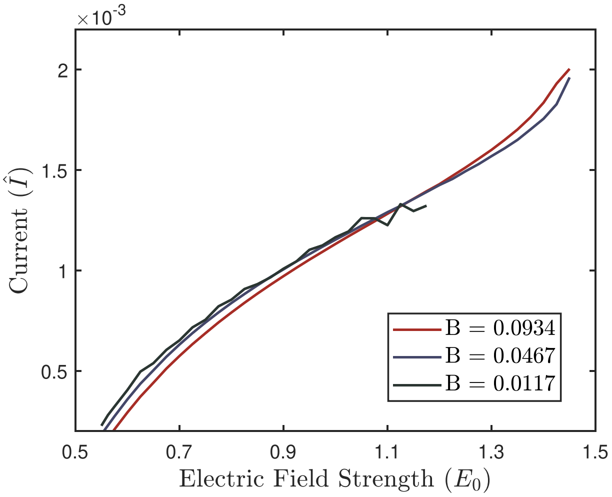

Fig. 6 The non-dimensional current relative to the extraction field strength (E_0) from the revised model at $C_R = 10^3$, $\hat{P}_r = 0$, and different meniscus ratios (B). This data shows the proportional relationship reported in the literature

magnitude from Gallud's implementation. Each of these solutions is a steady-state solution providing steady emission.

The previous and revised models generally exhibit the same trends [11, 14]. However, there are slight differences in the overall non-dimensional values between the revised and Gallud's model, outlined in Figs. 6 and 8. The trend lines for the hydraulic impedance of 10^3 have R^2 values of 0.98, 0.98 and 0.96 (for decreasing B). For the hydraulic impedance of 10^4, the R^2, values are 0.99, 0.99 and 0.99. While a linear regression is unlikely to truly represent emission trends (primarily at the onset and cessation of emission), it provides a metric for comparing the linearity of the trend to the experimental literature [11].

The relationship between the non-dimensional electric field and the non-dimensional current in Figs. 6 and 7 show $I-V$ proportionality when dimensioned. The difference in emission magnitude between each hydraulic impedance value also outlines the $I - C_R^{-1}$

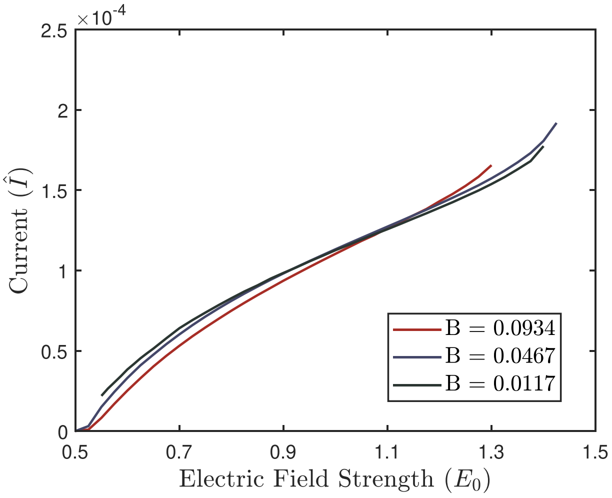

Fig. 7 The non-dimensional current presented relative to the extraction field strength (E_0) from the revised model at $C_R = 10^4$, $\hat{P}_r = 0$, and different meniscus ratios (*B*)

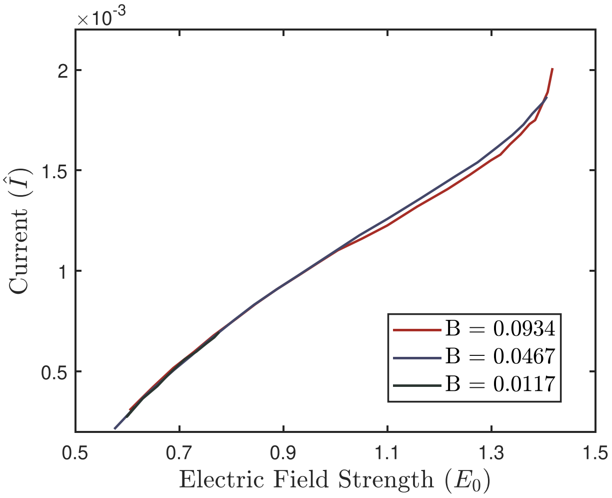

Fig. 8 The non-dimensional current relative to the extraction field strength (E_0) from Gallud's implementation at $C_R = 10^3$, $\hat{P}_r = 0$, and different meniscus ratios (*B*). This data aligns with the results produced from the revised model in Fig. 6. Data are extracted from Figures 4–6 [14]

proportionality of the revised model (Figs. 6 and 7). Also noted is the relatively close agreement of non-dimensional current for each parameter value of *B*. When this is converted to a dimensioned calculation for physical comparisons, it demonstrates increasing current for a decreasing *B*, emulating the physical process ($I - B^{-1}$ proportionality). Coffman's 'Relationship between stability and contact line' can be restated as an upper limit to E_0; this can be thought of in the same manner as Gallud's E_0 limit, which can be seen in the revised model. Finally, a non-emitting solution is presented in Fig. 9 to emulate previous validation. The existence of this solution is consistent with the findings of Coffman and Gallud, indicating the model replicates the expected outcomes [11, 14]. The revised model therefore demonstrates all the trends previous models used to compare to physical systems, demonstrating its similar practical relevance.

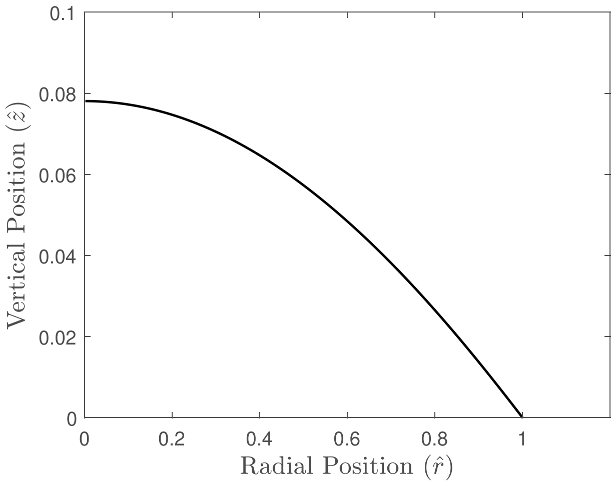

Fig. 9 Non-emitting solution at $C_R = 10^3$, $E_0 = 0.35$, $B = 0.05$, and $\hat{P}_r = 0$. The existence of this solution replicates physical implementations

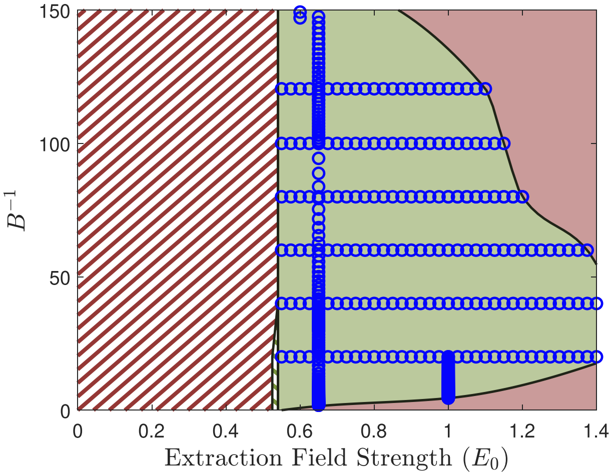

Fig. 10 The solution domain of the revised model at $C_R = 10^3$ and $\hat{P}_r = 0$. E_0 is non-dimensional field strength, and B^{-1} is a non-dimensional measurement of the radius of the liquid column. The blue circles represent numerical solutions. The shaded green zone is the region where emitting solutions are found, red is where no solutions are found, red hatched is where non-emitting solutions are found, and finally, green hatched is where both emitting and non-emitting solutions are found (considered to be the intermittent/pulsating mode by Coffman [11])

Solution space

The solution space comparison provides neither validation or verification, instead providing a comparison of the numerical stability between the previous and revised models [11, 14]. Two parameter sweeps from the revised model are presented in Figs. 10 and 11: these solutions have the B^{-1} ratio on the y axis and non-dimensional electric field on the x axis. Figure 12 presents the range of solutions for a hydraulic impedance of 10^3 found by Coffman. The parameter sweeps are for $\hat{P}_r = 0$. Notably, additional solutions are found for the revised model, and the zone for which both emitting and non-emitting solutions exist almost disappears for a C_R of 10^4.

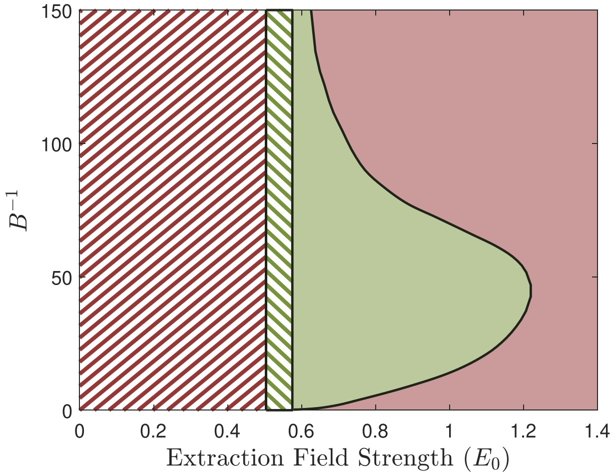

Fig. 11 The solution domain from Coffman's implementation at $C_R = 10^3$ and $\hat{P}_r = 0$. Compared to Fig. 10 the range of stable solutions is reduced. Data are extracted from Figs. 8–30 [11]. This figure uses the same symbols and colours as Fig. 10

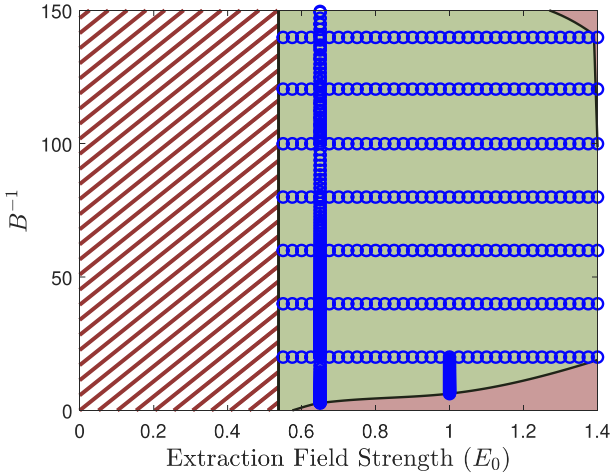

Fig. 12 The solution domain of the revised model at $C_R = 10^4$ and $\hat{P}_r = 0$. Compared to Fig. 10 the range of stable solutions has visually expanded. This figure uses the same symbols and colours as Fig. 10

Performance characterization

A comparison of the required number of iterations until solution for the revised model and Gallud's implementation are presented in Figs. 13 and 14, respectively.

There are multiple points of interest in Fig. 13. Firstly, the initial residual for the revised mode is lower than Gallud's implementation [14]. Secondly, the reduction of residual per iteration in the revised model follows a more traditional Newtonian solver trend with a logarithmic decrease in residual. This difference in error likely occurs due to how residuals were calculated. Since the previous residual was the maximum of one of three forces, the sudden change in the direction of the residual is likely represented by a change in the dominant residual pressure. Importantly, there is a significant reduction in the number of required iterations for a 'converged' solution to be found, at approximately five times smaller for each β value (increasing at smaller values of β).

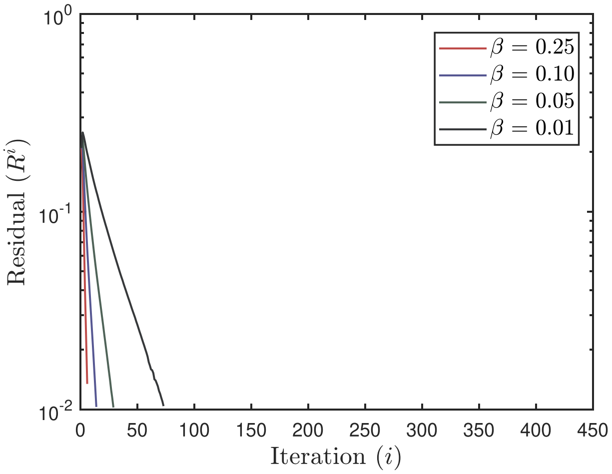

Fig. 13 Residual ($R^i = \Delta\hat{y}^i$) as a function of iterations for the revised model for various relaxation coefficients (β). Initial values are $C_R = 10^3$, $E_0 = 0.70$, B=0.0467, $\hat{P}_r = 0$, where E_0 has been increased to $E_0 = 0.75$ for the solution

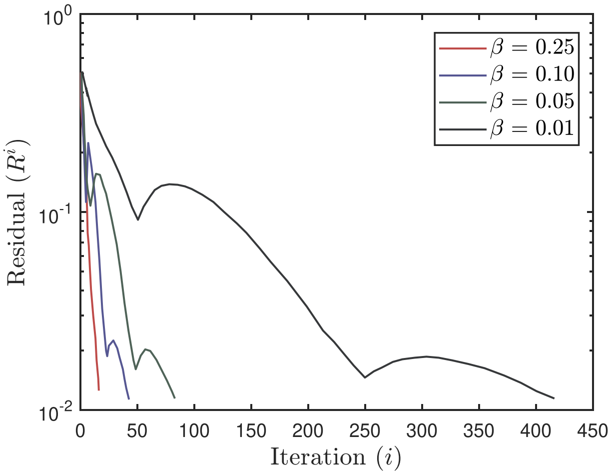

Fig. 14 Residual as a function of iterations for Gallud's implementation. Initial values are $C_R = 10^3$, $E_0 = 0.70$, B=0.0467, $\hat{P}_r = 0$, where E_0 has been increased to $E_0 = 0.75$ for the solution. Compared to Fig. 13, this implementation requires more iterations to converge. Data are extracted from Figs. 4, 5, 6, 7, 8, 9, 10, 11 [14]

Iteration duration

The number of CPUs and the quantity of RAM for the revised model is controlled through restriction of resources to a virtual computer. The time per iteration for the revised model can be seen in Figs. 15 and 16, Gallud's results are shown in Fig. 17.

Comparing Gallud's best-performing CPU allocation (four CPUs) to the revised model shows a slight performance increase, between an average of approximately 25 seconds per iteration for the previous implementation and an average of 17.8s for the revised implementation; this represents a time reduction of approximately 25%. Combining this decrease in iteration duration and the 80% decrease in the number of required iterations leaves a per-solution time reduction of 85%. The process is evidently not CPU bound.

As the number of cores does not limit the revised model, there are two other principle restrictions: RAM allocated to the model or the performance of a single CPU core. The investigation outlined in Fig. 16 shows the time required per iteration based on

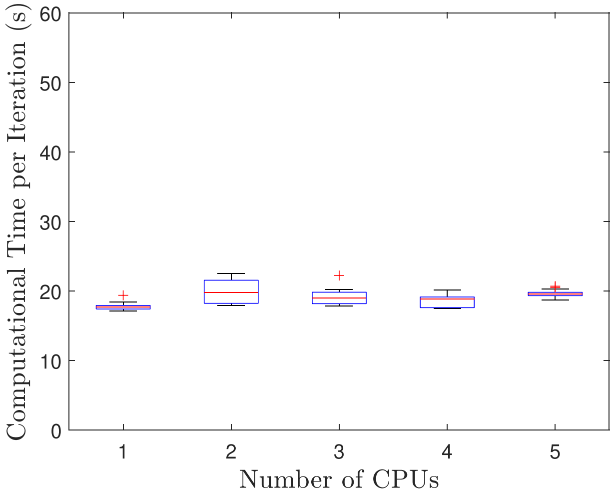

Fig. 15 Computational time per iteration as a function of CPU allocation for the revised model. Initial values are $C_R = 10^3$, $E_0 = 0.70$, B = 0.0467, $\hat{P}_r = 0$, where E_0 has been increased to $E_0 = 0.75$ for the solution

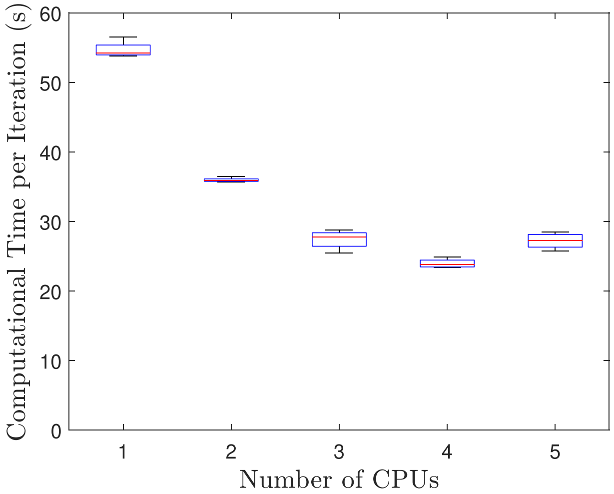

Fig. 16 Computational time per iteration as a function of CPU allocation for Gallud's implementation. Initial values are $C_R = 10^3$, $E_0 = 0.70$, B = 0.0467, $\hat{P}_r = 0$, where E_0 has been increased to $E_0 = 0.75$ for the solution. Compared to Fig. 15, each iteration is more computationally expensive. Data are extracted from Figs. 4, 5, 6, 7, 8, 9, 10, 11, 12 [14]

the allocation of RAM, showing that the quantity of RAM is not a performance-limiting parameter for the revised model. Generally, if the quantity of RAM allocated to the revised model is high enough to store the sub-models and required information, then it has little bearing on performance. The revised model used approximately 5.1 GB of RAM during operation. Consequently, the performance of a single core is the principal determining factor for iteration time.

Influence of thermodynamic properties

Impact of heat capacity and impact of thermal conductivity

The performance dependence on heat capacity and thermal conductivity are investigated at constant parameter values of $C_R = 10^3$, $E_0 = 0.65$, B = 0.05, $\hat{P}_r = 0$ and again at a higher field strength: $C_R = 10^3$, $E_0 = 1$, B = 0.05, $\hat{P}_r = 0$. Heat capacity (c_p) starts at 1500 J/kg-K and is increased until 4000 J/kg-K at the two selected single solutions (while

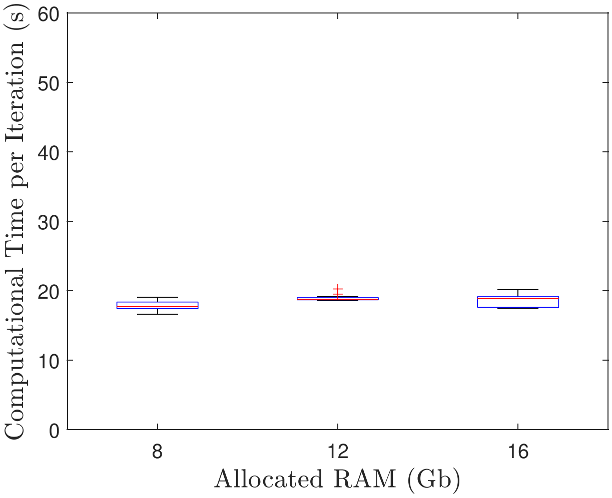

Fig. 17 Computational time per iteration for different RAM allocations for the revised model. Initial values are $C_R = 10^3$, $E_0 = 0.70$, B=0.0467, $\hat{P}_r = 0$, where E_0 has been increased to $E_0 = 0.75$ for the solution. No clear relationship between the variables is observed

thermal conductivity remained constant). Thermal conductivity is then increased from $k_T = 0.2$ W/m-K to $k_T = 0.6$ W/m-k at the two selected single solutions (while heat capacity remained constant). These investigations result in no significant change in non-dimensional current, contradicting the initial hypothesis.

Meniscus balance and emitted current

There is no evidence to support the hypothesis that these thermodynamic properties would impact the temperature at the emitting zone of the meniscus and, via Eq. 15, impact emission. Furthermore, an investigation of menisci temperature confirms that temperature distributions were significantly impacted by changes to these properties, with increased heat capacity lowering peak temperature by more than $2K$. From this, an 8% decrease in electrical conductivity would be expected. However, this appears to not affect the meniscus emission.

As with Gallud's electrical conductivity investigation, these temperature changes do result in some local changes in the meniscus contour, mainly at the tip [15]. However, far from the tip, the contour appears to be primarily controlled by upstream effects. To explain this, the balance outside the critical region is considered, where neither emission nor heating occurs. In this case, the external electric field and the upstream feed system completely define the surface tension. The electric field strength outside of the tip region experiences little amplification through the Taylor cone structure. Therefore, the electric traction is largely invariant to most effects, excluding external field changes. The surface tension is defined by a coherent boundary and all liquid forces are hydrostatic, consequently, there are limited curvatures that support the electric field traction gradients. Since the electric and surface tension forces remain the same, to maintain the equilibrium balance, the pressure drop due to the feed system must also remain the same, and therefore, emission must remain the same. Thus, it appears as though local tip changes exist to facilitate this required emission, that then supports the rest of the Taylor cone equilibrium.

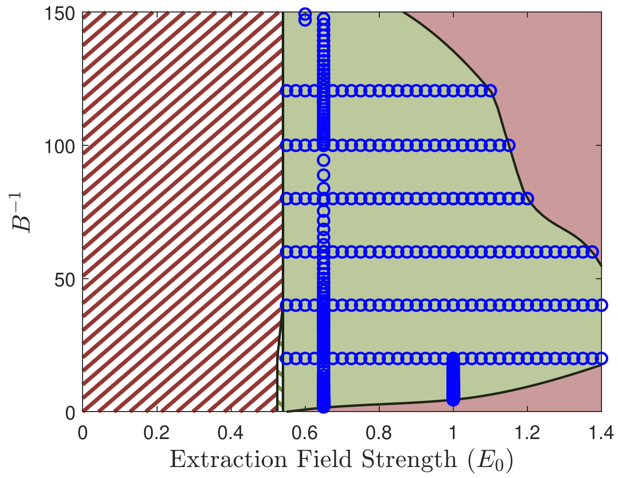

Fig. 18 The solution domain at $C_R = 10^3$, $\hat{P}_r = 0$, and $\alpha = 1.25 \times 10^{-7} m^2 s^{-1}$. This figure uses the same symbols and colours as Fig. 10

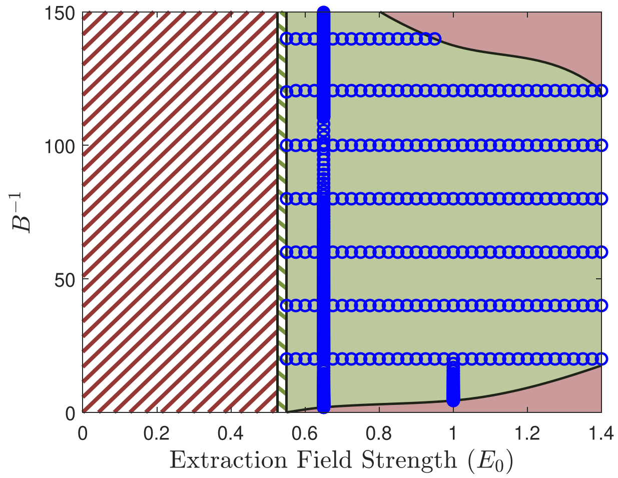

Fig. 19 The solution domain at $C_R = 10^3$, $\hat{P}_r = 0$, and $\alpha = 1.5 \times 10^{-7} m^2 s^{-1}$. Compared to Fig. 18 the range of stable solutions has visually expanded. This figure uses the same symbols and colours as Fig. 10

Impact of thermodynamic properties on solution range

Figures 18 and 19 present the range of stable solutions for *α* at values of $1.25e^{-7} m^2 s^{-1}$ and $1.5e^{-7} m^2 s^{-1}$. As with Gallud's 2023 work, the larger region of solutions can be interpreted as a more stable solution or model [15]. The numerical stability of these models is likely a reflection of physical meniscus stability, thus these results provide an indication of an increase in physical meniscus stability. However, the relationship between numerical and physical stability has only been demonstrated mathematically, and not practically [13]. In the case presented, the 20% increase in diffusivity allows for further solutions to be determined, broadly acting as a form of numerical stabilizer. This is to be expected as increased thermal diffusivity is equivalent to increased numerical diffusivity, which reduces spatial gradients.

The impact of thermal diffusivity on the stability of the revised model can be attributed to the traditional failure mechanisms, most notably current runaway. The increase in thermal diffusivity can be thought of as an increase in the ability of the liquid to dissipate excess energy faster; thus, when the revised model is perturbed (for example,

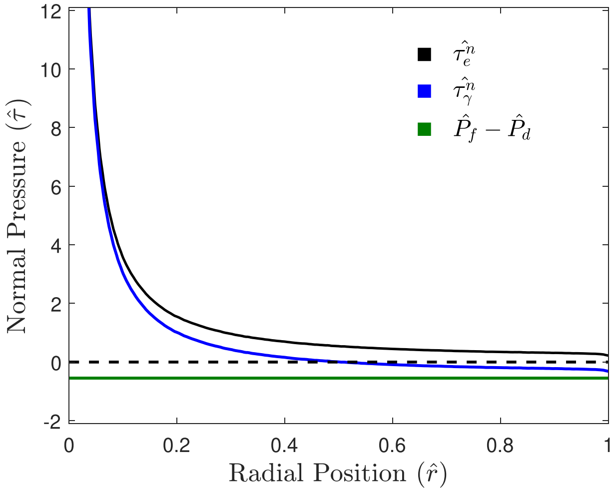

Fig. 20 The non-dimensional pressures at the meniscus at $E_0 = 0.65$, B=0.00467, $C_R = 10^4$, $\alpha = 1.5e^{-7}m^2s^{-1}$, and $\hat{P}_r = 0$. $\hat{P}_f - \hat{P}_d$ is constant over the meniscus. Compared to Fig. 4, the surface tension is significantly larger near the tip due to the tighter curvature

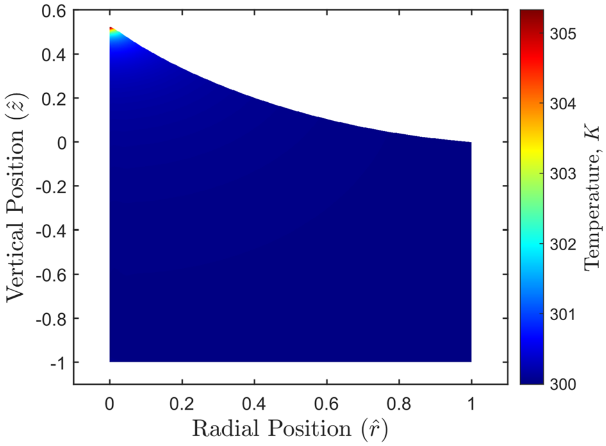

Fig. 21 The temperature distribution of the liquid domain at $E_0 = 0.65$, B=0.00467, $C_R = 10^4$, $\alpha = 1.5e^{-7}m^2s^{-1}$, and $\hat{P}_r = 0$. Compared to Fig. 5, the temperature gradient is more concentrated near the tip, reflecting the tighter meniscus curvature at the tip

as it propagates towards an equilibrium), it is more capable of tolerating force or heat imbalances.

Practical capillary size selected solution

As with experimental pure-ion electrospray emitters, these models often have more difficulty converging to emitting solutions at higher radii, where pressure gradients increase. Consequently, the maximum radii achieved by the previous models was restricted to a size of approximately $5\mu\text{m}$ [11, 25]. This starkly contrasts experimental reality, which often used approximately $10\mu\text{m}$ or larger capillary emitters [22, 26]. However, with the increased stability from the revised model, a higher diffusivity and a hydraulic impedance of 10^4, the revised model can produce a solution at approximately $10\mu\text{m}$ (translating to a parameter of B = 0.00467). The associated temperature and pressures are presented in Figs. 20 and 21.

The pressure values in Fig. 20 are more than an order of magnitude higher than those of the originally selected single solution, which explains the previous difficulty in solving these cases. This solution should allow for a feasible comparison with a corresponding physical experiment.

Discussion

Since the revised model exhibits the same validation trends as those reported by Coffman and Gallud, it is considered to be equally representative of the physical system [11, 14]. Problematically, this means that the revised model suffers the same validation gap as the previous models, where the absence of well-defined physical datasets hinders direct comparison with emission metrics from physical emitters, thereby forcing reliance on trend validation [15]. Meniscus images suffer from the same issue, where although their deformation appears visually similar to the predicted menisci from these models, uncertainty in the operating conditions restricts direct comparison [27]. Consequently, the physical accuracy of these results remains uncertain, and further research will be necessary.

These models remain in the early stage of development. Several physical processes remain poorly understood. For example, it is not known how the charge-to-mass ratio evolves with any parameter, forcing it to be specified for these models. Furthermore, for porous emitters (which are more standard in electrospray propulsion [28]), it is unknown what size the meniscus takes, where it is attached, and how different input parameters might cause these to change [15].

Furthermore, these electrohydrodynamic models are simplified and discretized representations of the real-world physics. In the revised model, the effects of space charge, convection of charged particles, and viscous liquid forces are all neglected. Although the omission of these effects is justified by existing literature [15], at specific parameters they may become more important. The kinetic evaporation law is also a simplified representation of activated emission; its presence is due to its simplicity and modeling heritage for both liquid metals and ionic liquids. However, as Coffman outlined, the kinetic evaporation law assumes that the charge layer at the meniscus surface is vanishingly small [11]. This assumption would hold if the free charges sat in small volumes between the components of the ionic liquid; however, for ionic liquids, the charges are attached to large molecules, therefore this is impossible.

Furthermore, as this modeling suggests, charge depletion is present at the meniscus; the effects of this are also unknown. This may change the liquid properties, and this depletion may not be sufficiently represented through the kinetic evaporation law. These simplifications are necessary, but they underscore the approximate nature of the models. A fundamental challenge is the lack of well-defined physical datasets for comparison, which forces reliance on trend-based validation. This issue is even more apparent for numerical stability. While Coffman and Gallud suggest that numerical stability either reflects or underestimates the physical stability of the electrospray meniscus, these conclusions remain tentative without further experimental validation [11, 15]. The fate of a collapsing meniscus also remains uncertain, whether this meniscus bifurcates, collapses, enters a intermittent mode, or whether this process is dependent on other factors.

Despite these limitations, these models continue to play a role in ongoing research. They are used as inputs for both molecular dynamics models, and emitter design optimization [29, 30]. Further research into the charge-to-mass ratio and porous emitters' attachment point is ongoing [27, 31]. Future adaptations and refinements of these models will be crucial to our understanding of the meniscus.

Comparison to earlier work

The demonstrated agreement between the revised and previous models allowed for the underlying verification of the implemented physics, and further highlighted the limited effects of the additional simplifications. However, all of these models are theoretical and corroborated solely with physical trends observed in the literature. Further validation is necessary to definitively demonstrate these models' relevance and generalizability.

Despite this, the revised model is expected to apply to the vast majority of pure-ion electrospray operating conditions, as is expected of previous models. However, the additional omitted physics will limit its relative generalizability to an extent. This is primarily evident when considering cone-jet operation. Previously, Gallud suggested that these models may also capture cone-jet behavior [15]. However, with the removal of viscous forces, momentum effects, and charge convection, the revised model is unlikely to represent cone-jet electrospray, where these effects play a more significant role. In the pure-ion regime, all available evidence and the results presented here indicate that these simplifications should not compromise physical relevance [11].

This can also be reinforced if one considered extreme parameters such as large meniscus sizes, where the liquid motion and viscous forces would increase in relative magnitude [15]. Even if the magnitude of these neglected viscous forces becomes substantial, their influence would remain localized near the meniscus tip. Based on both the present findings with thermodynamic properties, and Gallud's previous study on conductivity, this region does not appear to govern overall meniscus behavior and is unlikely to lead to notable changes in emission performance. Therefore, the underlying assumptions of the revised model are expected to remain valid even under extreme parameters.

The most significant omission that may restrict the scope of pure-ion emulation is space charge. Coffman argued, and Gallud later confirmed, that space charge is unlikely to alter meniscus behavior in general [11, 15]. Nevertheless, Gallud also found that if the hydraulic impedance decreases to approximately Mair's characteristic impedance, space charge can noticeably influence the meniscus [32]. As pointed out by Gallud, these conditions will represent an extreme rather than a general limitation, and overall, the model should remain broadly generalizable to pure-ion electrospray emission.

In terms of the primary disparity between the revised and previous models, this is denoted in Figs. 10 and 11, where the revised model presents more stable solutions, indicating that it is more numerically stable. This is unsurprising, given that much of the instability in the previous models stemmed from the highly non-linear coupling between the dynamic viscous forces and the electrostatic forces.

The additional solutions continue to fall within Gallud's identified non-dimensional field limit of approximately $\sqrt{2}$, supporting Gallud's analysis of a physical limit to stability [15]. Since the additional solutions continue to follow the physical trends identified by both Coffman and Gallud, it is impossible to determine if these solutions are physical, unphysical or even if the numerical instability of all three models has precluded the computing of further results, which may exist physically. Further validation is required.

The 'pulsating' regime's smaller solution region in the revised model was an unpredicted outcome. While the existence of multiple solutions for a non-linear model such as this is normal, its near disappearance in Fig. 10 indicates that it is a numerical feature of these models rather than something physical. However, this finding should be treated with caution until it is further validated experimentally. The likely explanation is the tightened convergence tolerance of the revised model. Because of the 'quasi-stable' nature of having two solutions, the non-emitting or emitting solution may not be numerically stable enough to be considered 'solved' under the tighter numerical scheme, resulting in their removal from the solution domain. This explanation requires more investigation, but it would add evidence to the idea that this zone is purely numerical.

Computational performance metrics

All five resource variations indicated negligible performance change based on the number of CPUs. Consequently, the revised model uses a single CPU for processing; assuming that Gallud used four cores, this reduces the hardware allocation by up to 75%. The lack of parallelization for the revised model could be due to inefficiencies in the implementation, the algorithm being inherently non-parallelizable, or the underlying problem itself being sequential. It could also be caused by virtual machine (VM) limitations. COMSOL should leverage multiple cores, but without the physical architecture of a single CPU socket, it could struggle with optimization, and it can face limitations due to the virtualized environment's restricted physical bandwidth [33, 34]. This lack of parallelization is not considered a problem for the revised model, as single CPU performance is higher than the reference model, and using a single core allows for a minimal allocation request from shared computing resources. Future researchers may be able to leverage parallelization for further performance gain.

Profiling of the revised model reveals that, approximately 20% of iteration time is spent loading or unloading models; this could be reduced with a faster SSD, a RAM drive, etcetera. Moreover, although Gallud provides a CPU clock speed of 2.7 GHz (compared to 2.65 Ghz for the server corers used in this work), direct comparisons through this method are not possible as memory bus size, cache size, and the architecture of a CPU all impact overall performance.

The data suggests that the revised model achieves a 85% decrease in per-solution time while requiring approximately 75% less computing resources. Furthermore, the revised models' increased linearity allows a consistent β selection of 0.1 for all meniscus sizes. This can be compared to Coffman and Gallud, who nominally used a value of 0.05 [11]. This relaxation parameter often decreased for higher values of B, making it difficult to quantify the increase in the numerical relaxation coefficient [35]. However, comparing their stated relaxation coefficient of 0.05 to the revised models' value of 0.1, provides a further per-solution time reduction of 50%.

Therefore, the revised model performs approximately 90% faster in terms of a single steady-state solution, while requiring 75% less computational resources per parallel implementation. These performance gains primarily originate from the reduced scope and degrees of freedom of the revised model, and are unlikely to be specific to the use of COMSOL. This conclusion is supported by the comparisons to Gallud's 2019 work [14], which employed a custom numerical implementation that was itself a more computationally efficient version of Coffman's 2016 COMSOL-based model (while encompassing the same physics) [11]. This suggests that further performance gains may be achieved through the development of fully customised software.

Impact of thermodynamic properties

Temperature fluctuations due to changes in the selected properties do result in some local changes in the meniscus shape, mainly at the tip, as with Gallud's investigation into conductivity [15]. However, the meniscus's overall shape and performance appear to be primarily defined by the upstream conditions, with changes in heat capacity and thermal conductivity not resulting in significant changes to emission. Apart from emission performance, an increase in diffusivity dramatically increases the stability of the numerical meniscus, indicating that a physical meniscus would also experience increased stability. This numerical stability allows the revised model to solve for a select solution at the larger and more common meniscus size of $10\mu\mathrm{m}$, potentially allowing future validation.

Conclusions

This work compares a revised model to the established results and trends in the literature, specifically focusing on Coffman and Gallud's work. The results show a good agreement with Coffman and Gallud [11, 14]. The revised model identifies additional numerically stable solutions beyond those previously reported, suggesting greater numerical stability due to improved handling of non-linear interactions between electrostatic forces and liquid effects. These new solutions are consistent with Gallud's non-dimensional field limits, necessitating further physical validation. The model reproduces the observed trends in the literature. This agreement suggests that the additional solutions may be physically plausible.

The revised model shows a significant improvement in performance over the Gallud's implementation with a 90% overall decrease in per-solution computational effort.

This additional numerical stability and performance that was found was leveraged to demonstrate the effects of varying individual thermodynamic properties, which were found to be insignificant. However, the impact on the numerical stability of the revised model by diffusivity was significant. The revised model was then used to produce solutions corresponding to a capillary radius of 10 $\mu\mathrm{m}$, permitting future physical comparisons.

Author contributions

F. Gooch conducted the research, developed the methodology, performed the analysis, and wrote the manuscript. J. Cater, K. Aw, and R. Sharma provided the initial conceptual advice, assisted with data analysis and interpretation, provided revisions to the manuscript, approved the final version, and agree to be accountable for all aspects of the work.

Funding

Open Access funding enabled and organized by CAUL and its Member Institutions. The authors did not receive support from any organization for the submitted work.

Data availability

The data that support the findings of this study are available from the corresponding author upon reasonable request.

Code availability

The code used in this study is the intellectual property of Ford Gooch and is not shared publicly. Access may be granted by the rights holder upon reasonable request.

Declarations

Competing interests

The authors have no conflicts to disclose.

Received: 9 August 2025 / Accepted: 9 February 2026

References

1. Krejci D, Lozano P (2018) Space propulsion technology for small spacecraft. Proc the Inst Electr Electron Eng 106(3):362–378
2. Krejci D, Mier-Hicks F, Fucetola C, Lozano P, Schouten AH, Martel F (2015) Design and characterization of a scalable ion electrospray propulsion system. In Proceedings of the 34th International Electric Propulsion Conference, Hyogo-Kobe, Japan
3. Levchenko I, Bazaka K, Ding Y, Raitses Y, Mazouffre S, Henning T, Klar PJ, Shinohara S, Schein J, Garrigues L (2018) Space micropropulsion systems for cubesats and small satellites: from proximate targets to furthermost frontiers. Appl Phys Rev 5(1):011104
4. Lozano P, Martinez-Sanchez M (2002) Experimental measurements of colloid thruster plumes in the ion-droplet mixed regime. In 38th American Institute of Aeronautics and Astronautics Joint Propulsion Conference & Exhibit, pp 3814
5. Adams A, Lozano P (2020) An investigation of nafion electrospray emitter tips. PhD thesis, Massachusetts Institute of Technology
6. Saville DA (1997) Electrohydrodynamics: the taylor-melcher leaky dielectric model. Annu Rev Fluid Mech 29(1):27–64
7. Higuera FJ (2003) Flow rate and electric current emitted by a Taylor cone. J Fluid Mech 484:303–327
8. Magnani M, Gamero-Castano M, Mora JF (2025) Determination of the characteristic length of electrosprays operating in the cone-jet mode. J Fluid Mech 1018, 5
9. Coffman CS, Martínez-Sánchez M, Lozano PC (2019) Electrohydrodynamics of an ionic liquid meniscus during evaporation of ions in a regime of high electric field. Phys Rev E 99(6):063108
10. Higuera F (2008) Model of the meniscus of an ionic-liquid ion source. Phys Rev E 77(2):026308
11. Coffman CS (2016) Electrically-assisted evaporation of charged fluids: fundamental modeling and studies on ionic liquids. PhD thesis, Massachusetts Institute of Technology
12. Wohlhuter FK, Basaran OA (1992) Shapes and stability of pendant and sessile dielectric drops in an electric field. J Fluid Mech 235:481–510
13. Coffman C, Martínez-Sánchez M, Higuera F, Lozano PC (2016) Structure of the menisci of leaky dielectric liquids during electrically-assisted evaporation of ions. Appl Phys Lett 109(23):231602
14. Gallud Cidoncha X (2019) A comprehensive numerical procedure for solving the taylor-melcher leaky dielectric model with charge evaporation. Master's thesis, Massachusetts Institute of Technology
15. Gallud Cidoncha X (2023) Studies on the physical structure, properties and operation of ionic liquid electrosprays in the pure-ion mode. PhD thesis, Massachusetts Institute of Technology
16. Castro S, Fernández De La Mora J (2009) Effect of tip curvature on ionic emissions from Taylor cones of ionic liquids from externally wetted tungsten tips. J Appl Phys 105(3):034903
17. Shamsipur M, Beigi AAM, Teymouri M, Pourmortazavi SM, Irandoust M (2010) Physical and electrochemical properties of ionic liquids 1-ethyl-3-methylimidazolium tetrafluoroborate, 1-butyl-3-methylimidazolium trifluoromethanesulfonate and 1-butyl-1-methylpyrrolidinium bis(trifluoromethylsulfonyl)imide. J Mol Liq 157(1):43–50
18. COMSOL AB: LiveLink for MATLAB User's Guide (2018) COMSOL AB, Stockholm, Sweden Version 5.4
19. The MathWorks, Inc. (2020) mATLAB user's guide. The MathWorks. Inc, Natick, Massachusetts, United States. The MathWorks, Inc. Version Rb
20. Gallud Cidoncha X, Kristinsson BO, Lozano PC (2019) Informing the design of pure-ion electrospray thrusters via simulation of the leaky-dielectric model with charge evaporation. In 36th International Electric Propulsion Conference
21. Krpoun R, Shea HR (2008) A method to determine the onset voltage of single and arrays of electrospray emitters. J Appl Phys 104(6)
22. Romero-Sanz I, Bocanegra R, Fernandez De La Mora J, Gamero-Castano M (2003) Source of heavy molecular ions based on Taylor cones of ionic liquids operating in the pure ion evaporation regime. J Appl Phys 94(5):3599–3605
23. Perez Martinez CS (2016) Engineering ionic liquid ion sources for ion beam applications. PhD thesis, Massachusetts Institute of Technology
24. Jegan B, Kumaraguruparam G, Kumar BV (2022) Investigation of thermo-physical properties of EMIMBF4 ionic liquid and water binary systems for heat transfer and refrigeration applications. Research Square Preprint
25. Lyne CT, Liu MF, Rovey JL (2023) A simple retarding-potential time-of-flight mass spectrometer for electrospray propulsion diagnostics. J Electric Propul 2(1):13
26. Suzuki K, Nagao M, Liu Y, Murakami K, Khumpuang S, Hara S, Takao Y (2021) Fabrication of nano-capillary emitter arrays for ionic liquid electrospray thrusters. Jpn J Appl Phys 60(SC):07
27. Donovan-Hill E, Turan N, Ryan C (2024) Direct optical visualisation of ionic liquid ion source Taylor cones. In 38th International Electric Propulsion Conference
28. Takeuchi M, Hamaguchi T, Ryuto H, Takaoka GH (2013) Development of ionic liquid ion source with porous emitter for surface modification. Nucl Instruments Methods Phys Res Sect B: Beam Interact Mater Atoms 315:345–349
29. Schroeder M, Gallud Cidoncha X, Petro E, Jia-Richards O, Lozano PC (2023) Inferring electrospray emission characteristics from molecular dynamics and simulated retarding potential analysis. J Appl Phys 133(17)
30. Smith A, Gallud Cidoncha X, Lozano P, Petro E (2024) Geometric and operating parameter modeling of electrospray arrays via multiphysics simulation. In 38th International Electric Propulsion Conference
31. Dworski S, Ryan C (2024) Analysis of plumes produced by novel ionic liquids in electrospray thrusters. In 38th International Electric Propulsion Conference
32. Mair GL (1997) The effects of flow impedance on the current-voltage characteristics of liquid-metal ion sources. J Phys D: Appl Phys 30(13):1945
33. Ionescu VM, Cazacu D (2015) Virtualization impact on COMSOL processor detection. Univ Pitesti Sci Bull Ser: Electron Comput Sci 15(2):25–32
34. COMSOL (2025) what hardware do you recommend for COMSOL Multiphysics? Online. Accessed: 06 Jan 2025
35. Gallud Cidoncha X (2021) Personal Communication. November 2021

Publisher's Note